DEGREE PROJECT IN TECHNOLOGY,
SECOND CYCLE, 30 CREDITS
STOCKHOLM, SWEDEN 2023

Localized and extended states in finite-sized mosaic Wannier-Stark lattices

KTH Master Thesis Report

Emrah Tortumlu

KTH ROYAL INSTITUTE OF TECHNOLOGY
DEPARTMENT OF APPLIED PHYSICS

Authors

Emrah Tortumlu <tortumlu@kth.se>
KTH Royal Institute of Technology

Place for Project

Department of Applied Physics, Division of Quantum Nano Photonics
School of Engineering Sciences
Stockholm, Sweden 2023

Examiner

Professor Val Zwiller
KTH Royal Institute of Technology

Supervisors

Associate Professor Ali W. Elshaari,

Dr. Jun Gao

KTH Royal Institute of Technology

Abstract

Anderson localization occurs when an otherwise conductive solid becomes insulating due to a sufficiently large degree of disorder in the medium. The electron band energy (as a function of disorder) at which this transition between extended and localized electron states occur is called the mobility edge (ME) and is energy-dependent only in 3-dimensional systems. In lower dimensional systems, energy-independent ME (all states localized or all extended) has been demonstrated by replacing disorder with quasi-periodic potential. However, recent theoretical findings indicate that neither disorder nor quasi-periodic potential is necessary for a material to exhibit electron localization and existence of energy-dependent pseudo ME at finite system size.

In this thesis work, we use light in coupled silicon nitride waveguides to simulate single-particle transport of a solid-state medium and investigate the coexistence of delocalized and localized states in disorder-free photonic lattices of finite system size. This was achieved by implementing a simulated linearly increasing electric potential on even-numbered sites by varying the refractive index of the wave guide (ch. 3). Through our experimental setup, we successfully achieved a coexistence of localized and delocalized states, where the degree of localization varies depending on the strength of the applied electric field.

The findings have implications for the field of quantum technology, where understanding and controlling quantum states is crucial. The ability to achieve localization in the absence of disorder opens new possibilities for designing and engineering photonic devices for quantum information processing tasks.

Keywords

Applied Physics, Condensed matter physics, quantum technology, quantum nanophotonics, localization, mobility edge, phase transition

Abstract

Anderson-lokalisering uppstår när ett annars ledande fast material blir isolerande på grund av en tillräckligt stor grad av oordning i mediet. Elektronbandsenergin (som en funktion av oordning) vid vilken denna övergång mellan förlängda och lokaliserade elektrontillstånd sker kallas mobilitetskanten (ME) och är energiberoende endast i 3-dimensionella system. I lägre dimensionella system har energioberoende ME (alla tillstånd lokaliserade eller alla förlängda) påvisats genom att ersätta oordning med kvasi-periodisk spänning. Nya teoretiska fynd indikerar dock att varken oordning eller kvasi-periodisk spänning är nödvändig för att ett material ska uppvisa elektronlokalisering och förekomsten av energiberoende pseudo-ME för system av finita storlekar.

I detta examensarbete använder vi ljus i kopplade vågledare av kiselnitrid för att simulera transport av en partikel i ett fast tillståndsmedium och undersöker samexistensen av icke-lokaliserade och lokaliserade tillstånd i finita system utan oordning med fotoniska gitter. Detta uppnåddes genom att implementera en simulerad linjärt ökande elektrisk potential på varje jämnt numrerat gitterläge plats genom att öka vågledarbredderna och noll elektrisk spänning på varje udda. Genom vårt experimentella upplägg lyckades vi uppnå lokaliserade och förlängda tillstånd, där graden av lokaliseringen varierade beroende på styrkan av det tillämpade elektriska fältet.

Fynden har implikationer för kvantteknologi, där förståelse och kontroll av kvanttillstånd är avgörande. Förmågan att uppnå lokalisering i frånvaro av oordning öppnar nya möjligheter för att designa och konstruera fotoniska enheter för kvantinformationsprocesser.

Nyckelord

Tillämpad Fysik, Kondenserade materiens fysik, kvantteknologi, kvantnanofotonik, lokalisering, fasövergång

Acknowledgements

I would like to take this opportunity to express my heartfelt gratitude to all those who have supported me throughout the course of my master's journey. Completing this thesis would not have been possible without the encouragement, guidance, and assistance of numerous individuals and institutions, and I am truly indebted to them.

First and foremost, I am deeply grateful to my thesis advisors, Associate Prof. Ali Elshaari and Dr. Jun Gao, for their unwavering support, invaluable insights, and dedication to my academic growth. Their mentorship and expertise have been instrumental in shaping the direction of this thesis work, and I am fortunate to have had the opportunity to work under their guidance.

I am also indebted to the staff and researchers at Quantum Nano Photonics group at the Applied Physics department of KTH, who provided me with valuable resources, technical assistance, and access to research materials.

Finally, I want to thank all the participants and respondents who took the time to contribute their insights and data, without whom this research would not have been possible.

Completing this master thesis has been a transformative experience, and I am grateful to everyone who played a role in making it a reality. Each person and institution mentioned above has had a profound impact on my academic and personal growth, and for that, I will forever be thankful.

Acronyms

DOS	density of states
ME	mobility edge
WSL	Wannier-Stark ladder
AAH	André-Aubry-Harper
IPR	inverse participation ratio
FDFT	finite-difference time-domain
CCD	charge-coupled device
SNSPD	superconducting nanowire single-photon detector

Contents

1 Introduction **1**

1.1 Background 1

1.2 Purpose 3

1.3 Outline 3

2 Theoretical Background **4**

2.1 Dynamics of Band Electrons in Electric Fields 4

2.1.1 Crystal Lattices 4

2.1.2 Wannier-Stark Lattice 6

2.2 Localization & Mobility Edge 8

2.2.1 Anderson Localization 8

2.2.2 Disorder-free localization 10

3 Methods **12**

3.1 Chip Design Parameters 13

3.2 Photonic Mosaic Lattice Fabrication 16

3.3 Experimental Procedure 17

3.4 Data Analysis Method 18

3.5 Differences in device structures 20

4 Result **22**

4.1 Theoretical solutions 22

4.2 Light Intensity Profile 22

4.2.1 Weak-force Regime 23

4.2.2 Strong-force regime 23

5 Discussions & Conclusions **26**

5.1 Discussion 26

5.2 Conclusion 28
5.2.1 Future Work 28

References **30**

Chapter 1

Introduction

Quantum technology is an emerging field of physics and engineering that is based on quantum theory and has many sub-fields, including quantum information science [1]. The 2022 Nobel Prize winners, Alain Aspect, John. F. Clauser and Anton Zeilinger are considered to be pioneers of quantum information science, as they experimentally proved the non-local correlation between two entangled particles, a property which is important for quantum technology [2, 3], and thus paving the way for technological advancements [4, 5]. However, information in the form of quantum states is very susceptible to environmental perturbations, or noise. This is one of the main challenges in advancements of quantum technology [5, 6]. Researchers working with quantum technology often refer to condensed matter physics as an approach to solving the issues related to noise in quantum technology, as well as finding new materials, and novel methods and integration techniques [3, 5, 7–13]. For example, there is on-going research on using topology to create topologically protected states in topological insulators to be used as qubits, making them more robust against environmental perturbations [14]. Clearly, theoretical findings has significant value for research of applied sciences, and experimental verification and observation of new theory is the bridge between the two.

1.1 Background

An interesting concept in condensed matter physics is the Anderson localization, named after Philip W. Anderson who described that electrons in a crystal lattice can become localized, i.e. remain in a local area of the lattice, and therefore cause a

material to become insulating as a result of crystal lattice disorder. This effect is distinct from the band gap theory of insulators - Anderson localization cause materials that are otherwise metallic in their band structure to become insulators. The source of localization is thought to be due to disorder in the lattice system, which can be achieved in various ways, for example from impurities in semiconductors [15].

The dimension of the system is important. In one and two-dimensional systems (1D and 2D), the states are all localized, regardless of how weak the disorder is. However, in 3D, localization occurs as a metal-insulator phase transition, which can be illustrated in Fig. 1.1.1. When the Fermi energy E_F is below the critical energy E^* (or above $E^{*'}$), also known as the mobility edge (ME), the electrons are localized, while above the ME (below) they are extended. Thus, the ME is a point at which the material undergoes a phase transition from insulating to conducting phase [16].

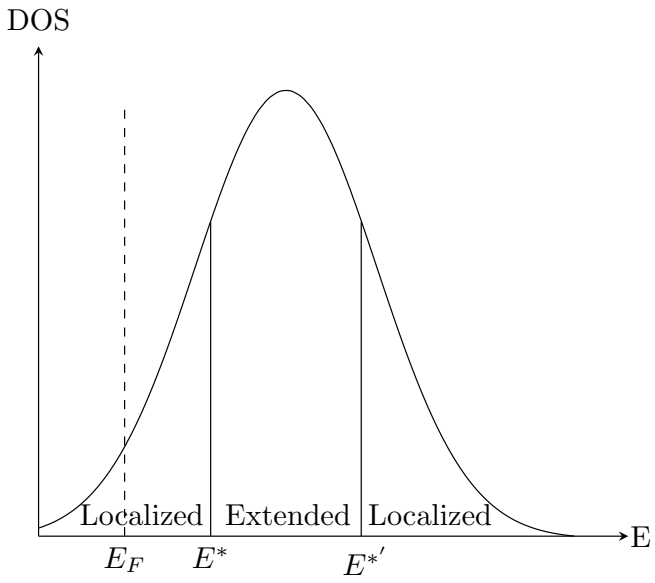

Figure 1.1.1: Illustration of the critical energy E_c, the mobility edge, at which a metal-insulator phase transition occurs in a 3D system with the disorder. The image is a recreation from *Modern Condensed Matter* by Steven M. Girvin and Kun Yang (2019), Fig. 11.15 p. 291.

Even though one and two-dimensional systems lack ME as a function of disorder, Dwiputra et al. have shown that a disorder-free[1] a pseudo mobility edges is possible in a finite 1D system [18]. A 1D tight-binding Hamiltonian model (Eq. 2.12) with the Stark effect in a mosaic lattice is solved to find pseudo MEs (Section 2.2.2).

While the main focus of localization in condensed matter physics is on that of electrons,

[1]Dwiputra et al. [17] define a disorder-free lattice as one lacking random or quasi-randomness.

the phenomenon is not limited to electrons. In fact, many phenomena in condensed matter physics have an analogy in optics and photonics [19]. For example, Anderson localization has been experimentally observed in a 1D disordered lattice of photonic waveguides [20]. While Anderson localization had been demonstrated previously, the methods were indirect via macroscopic properties, e.g. via conductance, back-scattering and transmission. The advantage of using photonic lattices is that it is possible to observe directly the suppression of the wave packet expansions of the particles due to localization [20].

1.2 Purpose

The purpose of this thesis work is to experimentally investigate the existence of localized and delocalized electron states in a 1D disorder-free mosaic lattice under a constant electric field as proposed by Dwiputra et al. [17] for both strong and weak electric fields. The scope of the experiment is limited to finite-sized lattices and will be carried out using photonic lattices with classical light to simulate electron states.

1.3 Outline

In Chapter 2 a more in-depth theory of several concepts that are important for this thesis work are presented, including mathematically explicit description of Anderson localization, the André-Aubry-Harper (AAH) model and a summary of the derivation of the ME for the disorder-free Wannier-Stark mosaic lattice as described by Dwiputra et al. [17]. In Chapter 3, the use of photonic lattices and how they can be used to simulate quantum transport of electrons will be described, along with a description of the engineering process of manufacturing the nanostructure, the experimental procedure, data analysis using image processing, and lastly two sections dedicated to discussions and conclusions.

Chapter 2

Theoretical Background

In this chapter, we describe the theoretical background that is necessary to understand for the goal of the thesis project. The first section (2.2) explains the concept of localization, starting with localization due to disorder as described by Anderson in 2.2.1 and continues with the description of disorder-free localization in 2.2.2.

2.1 Dynamics of Band Electrons in Electric Fields

This section focuses on a brief review of band theory and electron mechanics under electric fields from the basis of crystal lattice structures.

2.1.1 Crystal Lattices

When discussing electrons in condensed matter physics, it is important to take into account the crystal structure of the atoms in the material in which the electron moves. A *crystal* is a structure with *translational symmetry*. This means that, knowing the positions of a few atoms, we can pin-point the positions of all the other atoms. This can be explained mathematically using *Bravais lattices*, which are discrete points in space with translation symmetries. In 3D, the Bravais lattice can be described as the set of points described by the *lattice vector* $\vec{\rho}$, where

$$\vec{\rho} = l\vec{a} + m\vec{b} + n\vec{c}. \tag{2.1}$$

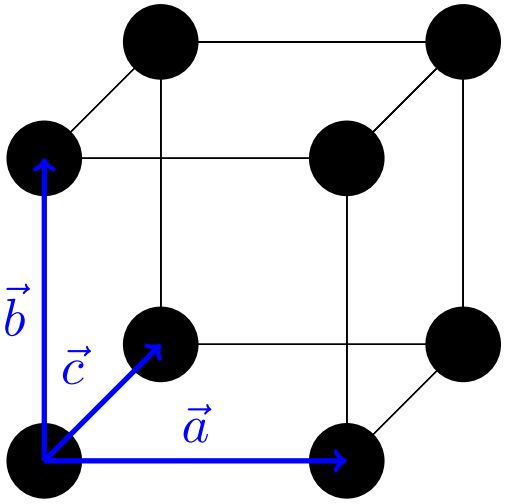

Figure 2.1.1: A simple cubic crystal with primitive lattice vectors $\vec{a} = a\vec{x}, \vec{b} = a\vec{y}$ and $\vec{c} = a\vec{z}$, where a is the *lattice parameter*.

Here, l, m, n are integers and $\vec{a}, \vec{b}$ and $\vec{c}$ are called *primitive lattice vectors*. As an example, a simple cubic crystal (SCC) is shown in Fig. 2.1.1 along with the primitive lattice vectors.

Owing to the translational symmetry, we can define *lattice translation operators* $T(\vec{\rho}) = \exp\left\{(i\vec{k} \cdot \vec{\rho})/\hbar\right\}$ satisfying $T(\vec{\rho})\,|\psi(\vec{x})\rangle = |\psi(\vec{x} + \vec{\rho})\rangle$, where $\vec{k}$ is the wave vector. Since we regard the crystal in which the electron moves as infinite, and that the crystal has a periodicity, an electron at position $\vec{x}$ is equivalent to an electron at position $\vec{x} + \vec{\rho}$. Thus, the Hamiltonian $\mathcal{H}_0$ of an electron will satisfy

$$\mathcal{H}_0(\vec{p}, \vec{x} + \vec{\rho}) = \mathcal{H}_0(\vec{p}, \vec{x}), \tag{2.2}$$

making $T(\vec{\rho})$ the constants of motion.

Additionally, $\mathcal{H}_0$ and $T(\rho)$ commute, making them simultaneously diagonalizable. We can therefore find a set of eigenvalues of the generating elements $T(\vec{a}), T(\vec{b})$, and $T(\vec{c})$, let them be $e^{2\pi i\lambda}, e^{2\pi i\mu}$ and $e^{2\pi i\nu}$. Thus, we have that

$$\vec{k} = 2\pi\{\lambda\vec{a}^* + \mu\vec{b}^* + \nu\vec{c}^*\}, \tag{2.3}$$

where $\vec{a}^*, \vec{b}^*$ and $\vec{c}^*$ are the *reciprocal lattice vectors* satisfying

$$\vec{a}^* = \frac{\vec{b} \times \vec{c}}{\vec{a} \cdot \vec{b} \times \vec{c}}, \tag{2.4a}$$

$$\vec{b}^* = \frac{\vec{c} \times \vec{a}}{\vec{a} \cdot \vec{b} \times \vec{c}}, \tag{2.4b}$$

$$\vec{c}^* = \frac{\vec{a} \times \vec{b}}{\vec{a} \cdot \vec{b} \times \vec{c}}. \tag{2.4c}$$

Similar to the lattice vector, we can form a *reciprocal lattice vector* using the primitive reciprocal lattice vectors, $\vec{G} = l\vec{a}^* + m\vec{b}^* + n\vec{c}^*$.

2.1.2 Wannier-Stark Lattice

Depending on the type of material, one may use different models to describe the electron inside the crystal structure. For example, in a highly conductive material, the electrons can be regarded as nearly free electrons. In crystal structures where the atoms are farther away and the electrons do not move as freely, one can use the tight-binding method to describe the electrons. In both of these cases, so-called Bloch functions are important.

Bloch functions are eigenfunctions of Hamiltonians with the same periodicity as the crystal, such as Eq. (2.2). Bloch's theorem tells us that these Bloch functions are the most general solutions of the periodic Schrödinger equation, and have the form

$$\psi_{\vec{k}} = e^{i\vec{k}\cdot\vec{r}} u_{\vec{k}}(\vec{r}) \tag{2.5}$$

where $u_{\vec{k}}$ is a periodic function having the translational symmetry of the lattice, and has the form

$$u_{\vec{k}}(\vec{r}) = \sum_{\{\vec{G}\}} a_{\vec{G}}(\vec{k}) e^{i\vec{G}\cdot\vec{r}}. \tag{2.6}$$

When using tight-binding methods, it is convenient to use functions describing the electrons based on their orbitals, which are called *Wannier functions*. The Wannier

function for a band n centered on the j-th unit cell is given by

$$|\chi_{nj}\rangle = \frac{1}{\sqrt{N}} \sum_{\vec{q}} e^{-i\vec{q}\cdot\vec{R}_j} |\psi_{n\vec{q}}\rangle ,$$

where $|\psi_{n\vec{q}}\rangle$ is the Bloch state for the n-th band.

Because Bloch functions only defined up to an arbitrary $\vec{q}$-dependent phase, different phases will give different Wannier functions. It is therefore possible, for ordinary bands (i.e. topologically trivial bands), to choose a phase that maximally localizes the Wannier function, and thus one can always find Wannier functions that are exponentially localized [21].

Since Eq. 2.2 arises due to the translational symmetry of the crystal lattice, if we introduce a uniform electric field E, the periodicity no longer holds. That is, an electron at the point $\vec{x}$ will no longer be described by the same Hamiltonian as one at the point $\vec{x}+\vec{\rho}$. This is what Gregory H. Wannier described in his paper in 1962, providing with a solution of the eigenenergy and eigenfunction to the Wannier functions in an external electric field [22]. Adding an electric potential term to the Hamiltonian,

$$\mathcal{H} = \mathcal{H}_0 - e\vec{E} \cdot \vec{x}, \tag{2.7}$$

he showed that the eigenenergies are

$$\epsilon_{qn} = E_0 + neE/a^* \tag{2.8}$$

where $\vec{a}^*$ is a period of the periodic lattice along the electric field and E_0 is the mean energy of the band. Since $1/a^*$ is the distance between the lattice planes perpendicular to E, we obtain equally-spaced energy levels in Eq. (2.8), referred to as the Wannier-Stark ladder (WSL). The eigenstates are exponentially localized and can be determined exactly as [23]

$$|m\rangle = \sum_n \mathcal{J}_{n-m}(2J/F) |n\rangle , \tag{2.9}$$

where $\mathcal{J}_\nu(z)$'s are the Bessel functions of the first kind, J is the hopping strength and F is the constant force. The existence of the WSL have been experimentally shown in superlattices [24, 25].

2.2 Localization & Mobility Edge

2.2.1 Anderson Localization

In a metal, it is possible to create an electrical current for example with a voltage difference between one end of the metal to the other, using Ohm's law. Conductance, which is the inverse of resistivity, describes how easily the electrons can move through the conducting material. While Ohm's law is a well-known relation between resistance, voltage and current, there has been a lot of interest in describing conductivity in more detail, specifically a quantum description of transport. One such model is the Einstein relation for conductivity, which relates electron conductivity σ with the combined (including both spins) density of states (DOS) per unit volume at the Fermi level for non-interacting electrons at zero temperature, $\frac{dn}{d\mu}$, and the diffusion constant D [16]:

$$\sigma = e^2 \frac{dn}{d\mu} D. \tag{2.10}$$

An insulator, defined by its lack of conductivity, has $\sigma = 0$. This can be achieved in two ways, either $\frac{dn}{d\mu} = 0$ or $D = 0$.

Based on the band structure theory of materials, insulators have zero conductivity due to the large band gap between the valence and the conducting bands, requiring a lot of energy to move the electron from one band to another. A semiconductor also has a band gap, however it is smaller than that of an insulator. For metals, on the other hand, the valence and conduction bands overlap, and thus electrons can move from one band to another in an infinitesimally small energy difference (see Fig. 2.2.1). The band theory of insulators can be related to the Einstein relation (Eq. 2.2.1) by the fact that band insulators satisfy $\frac{dn}{d\mu} = 0$ (and thus $\sigma = 0$), since the DOS at Fermi level for the electrons is zero.

However, as evident by Eq. 2.2.1, there is another parameter than can cause a material to be an insulator while $\frac{dn}{d\mu} > 0$, the diffusion constant D. The constant D can be zero when the electron eigenstates are localized, i.e. they are confined and do not extend in long distances. When such a localization is caused by disorder in the material, it is commonly referred to as **Anderson localization**, named after Philip W. Anderson, and the origin of the effect is quantum interference [15]. The disorder in the metal causes the electron wave function to be trapped within a fixed distance called the **Anderson localization length** ξ. In 1 and 2 dimensional systems, all electron

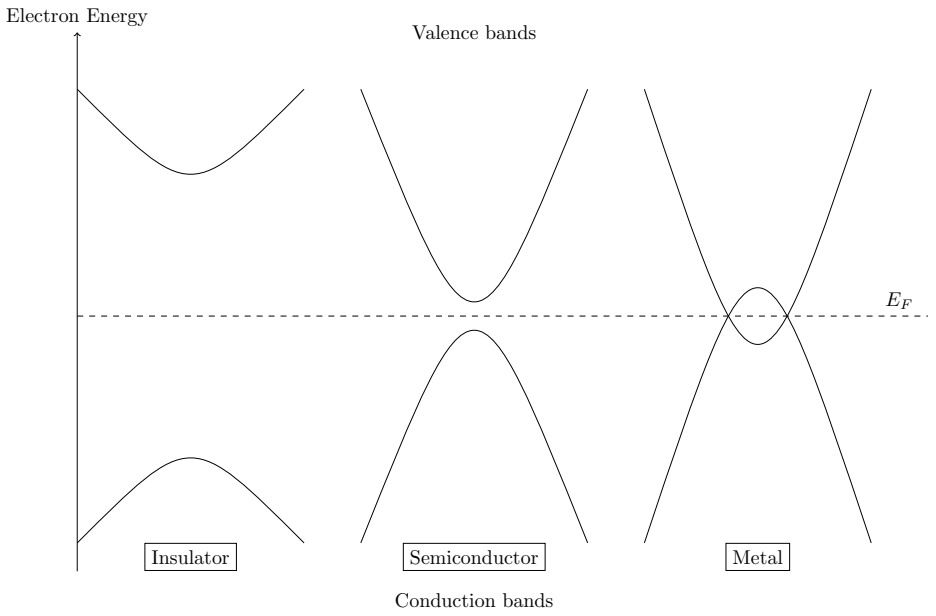

Figure 2.2.1: Illustration of the band structure theory of metals, insulators and semiconductors. The Fermi level E_F is in the middle in all these cases for simplicity.

eigenstates are localized, no matter how weak the disorder is, as described by the scaling theory [26].

While Anderson localization (due to random disorder) in one and two-dimensional systems lack MEs, there are several methods of achieving a ME in 1D systems by using *incommensurate lattices*, i.e. a lattice with two periodicities and where the ratio between the two periods is an irrational number. The simplest non-trivial model with a 1D incommensurate lattice is the AAH model, which shows a metal-insulator phase transition due to localization when varying disorder strength. In this case, however, the phase transition is independent of energy, and thus lacks ME.

The MEs in incommensurate lattices can be introduced in various ways, such as by varying on-site potential [27, 28], introducing long-range hopping [29], or by a *mosaic lattice* with equally-space zero-potential sites [30]. However, as described by Dwiputra et al. [17], neither random disorder nor quasiperiodic potentials are necessary to achieve a a pseudo ME. This is further described in 2.2.2.

Inverse Participation Ratio

A method for distinguishing localized from extended states is the inverse participation ratio (IPR), an integral over the amplitude of the state function, and depends on the

dimension of the system:

$$P_q = \int d^d r |\Psi(\vec{r})|^{2q}, \tag{2.11}$$

where q is a parameter.

Low values of P indicate extended states, while P close to 1 indicates highly localized states. This can be used to calculate the degree of localization, such as in Fig. 2.2.2

2.2.2 Disorder-free localization

A pseudo ME for a finite 1D disorder-free mosaic lattice with Stark effect is described by Dwiputra et al. [17], where the notion of disorder-free refers to "absence of the random or quasi-randomness". S. Longhi [18], showed that Avila's global theory cannot be applied here and Lyapunov exponents cannot be defined for Stark potentials, going to infinity. In the thermodynamic limit (when the system size goes to infinity), all states become localized with the exception of few isolated extended states, thus strictly speaking no disorder-free ME exists. Only under a finite-height mosaic potential [31], can the Wannier-Stark lattice manifest a pseudo ME, which can be experimentally realized and probed.

To show this, a 1D tight-binding Hamiltonian model is used with Stark effect and the so-called mosaic lattice [30] of length L and parameterized by an integer κ:

$$\mathcal{H} = -\mathcal{J} \sum_n (c_n^\dagger c_{n+1} + H.c) + \sum_n \epsilon_n c_n^\dagger c_n, \tag{2.12}$$

$$\epsilon_n = \begin{cases} Fn, & n = \kappa l, \\ 0, & \text{otherwise.} \end{cases} \tag{2.13}$$

Here c_n is the annihilation operator at site n, $\mathcal{J}$ is the nearest-neighbor hopping, F is a constant force, and $l = 0, ..., N-1$ is an integer.

With this model, we have a chain of lattices with Stark potential on every κ-th site, and zero potential otherwise.

By studying separately the localized wave functions, having most of their weight at $n = m\kappa$ sites, decaying faster than exponentially with distance, and large energies

$E_m \simeq Fm\kappa \gg 1$ with the perturbation theory in J/E_m and the corresponding effective Hamiltonian with the projected out above localized states [32], we have improved the results of [17], finding the following pseudo ME.

$$E = E_{ME} = \max\left[2J, \left(\frac{eJ}{F\kappa L}\right)^{1/(\kappa-1)}\right] . \tag{2.14}$$

In Fig. 2.2.2, the numerical solutions of the pseudo MEs for $\kappa = 2, 3, 5, 6$ have been plotted along with the respective IPR. The IPR analysis shows highly localized states (black lines) and extended states (yellow dotted lines) on either side of the exact ME (red dashed line).

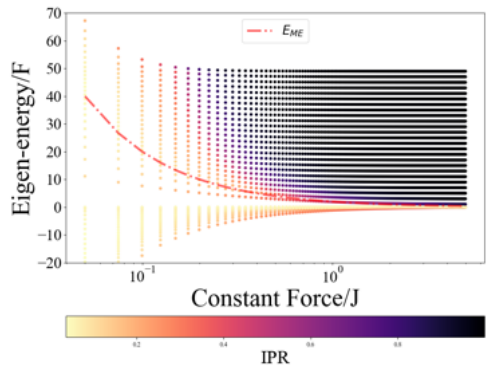

(a) $\kappa = 2$

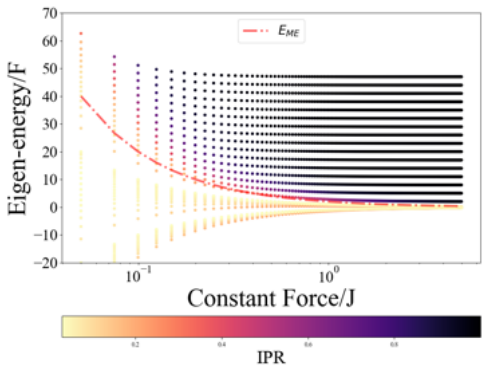

(b) $\kappa = 3$

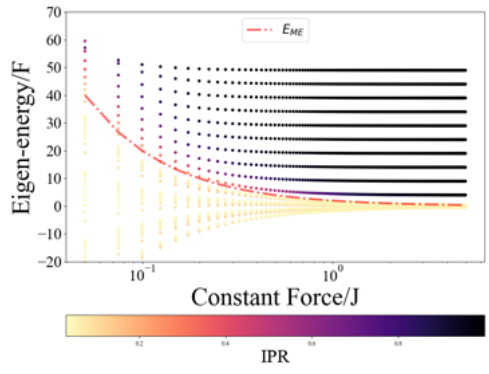

(c) $\kappa = 5$

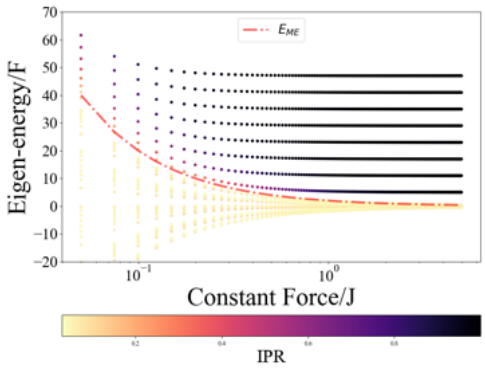

(d) $\kappa = 6$

Figure 2.2.2: IPR and exact ME with $L = 50$ sites for (a) $\kappa = 2$, (c) $\kappa = 3$, (d) $\kappa = 5$, and (e) $\kappa = 6$.

Chapter 3

Methods

Photonic structures have previously been used as analogies to quantum phenomena in for example condensed matter physics due to the similarity between wave-like functions of e.g. electrons and the classical waves of light [19]. It can be shown that the Schrödinger equation describing an electron in a potential $V(x)$ with a time-dependent wave function (for simplicity, we allow only a transverse spatial coordinate x, but this can be easily extended to two transverse spatial coordinates x, y),

$$-\frac{\hbar^2}{2m}\nabla^2\Psi(x,t) + V(x,t)\Psi(x,t) = i\hbar\frac{\partial}{\partial t}\Psi(x,t) \tag{3.1}$$

is similar to the optical paraxial Helmholtz equation,

$$i\lambda\frac{\partial}{\partial z}E(x,z) = (-\frac{\lambda^2}{2n_0}\frac{\partial^2}{\partial x^2} + \Delta n(x,z))E(x,z) \tag{3.2}$$

which describes the propagation of classical light with wavelength λ through a waveguide along the z-direction, where Δn is the refractive index profile of the guiding structure and n_0 is the reference (substrate) refractive index. This similarity allows for the simulation of the quantum effects of electrons in lattices to be simulated using photonic lattices with waveguides, where the temporal part of the electron wave function is replaced by the spatial propagation of classical light in the z-direction, as well as simulating a potential in the Schrödinger equation (3.1) by adjusting the effective refractive index in the waveguides. This is central in this thesis work, as we will be using photonic lattices to simulate the model described in Eq. (2.12) with classical light. Moreover, the experimental procedure will be limited to finite-sized lattices as

opposed to the theoretically-derived case of thermodynamic limit (where the system size $N \to \infty$).

In the following sections, the necessary chip design parameters (sec. 3.1) and the fabrication design of the photonic mosaic lattice are described (sec. 3.2). The last two sections describe the experimental procedures 3.3 and the data analysis method used in the thesis 3.4.

3.1 Chip Design Parameters

Before fabricating the chip, it is necessary to design the chip parameters correctly. Firstly, to achieve the WSL, it is necessary to have a linearly increasing electric field in every κ-th site, and with a fixed coupling constant $\mathcal{J}$ between the lattices. Since in we use $\kappa = 2$ in this experiment, we need the linearly increasing electric field on every second site (even sites), and zero field on every odd site, see Fig. 3.1.1.

The modelling and approach of finding coupling constants follows the methods developed by Stefan Nevlacsil, et al. [33]. The odd-site zero-field was achieved by keeping the waveguide widths of the odd sites constant at 550 nm. The on-site energy of each individual waveguide was calculated using

$$\beta_n = \frac{2\pi}{\lambda} n_{eff}(\lambda), \tag{3.3}$$

where n is the site number, λ is the wavelength of the light source propagating in the waveguide, and n_{eff} is the effective refractive index in the waveguide.

To find the effective refractive index, finite-difference time-domain (FDFT) was implemented using Ansys Lumerical. The initial model, consisting of a single SiN waveguide with refractive index of 1.96 is laid on top of an insulating SiO_2 with a refractive index of 1.459 (see Sec. 3.2). Since a 810 nm light source will be used for the actual experiment, a source in the simulation with wavelength interval of $(0.8085 - 0.8115)\,\mu$m was chosen, see Fig. 3.1.2a.

By running a mode simulation of the waveguide near its refractive index, we receive a plot of the electrical field intensity as well as an effective refractive index, see Fig. 3.1.2b.

The waveguide width is varied within an interval $0.35 - 0.90\,\mu$m with an incremental

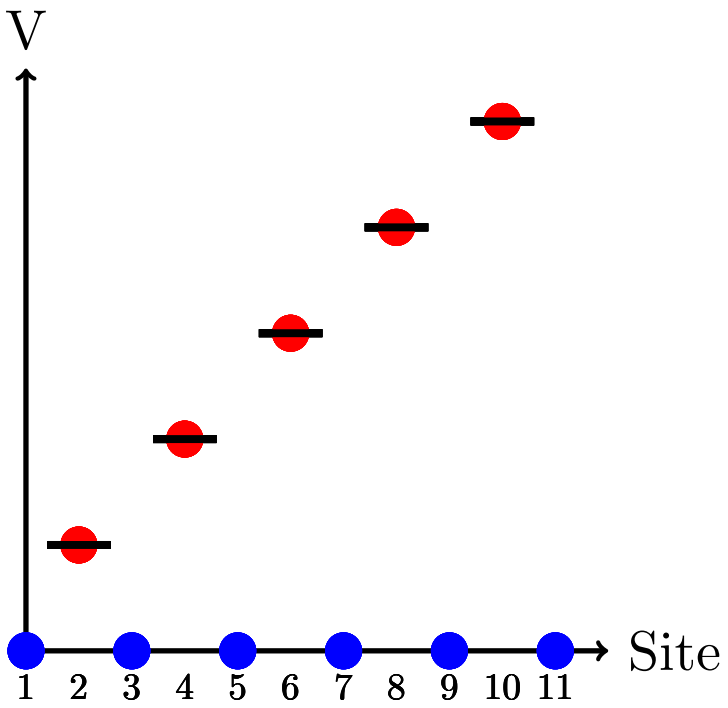

Figure 3.1.1: Illustration of the linearly increasing electric potential in the WSL with $\kappa = 2$.

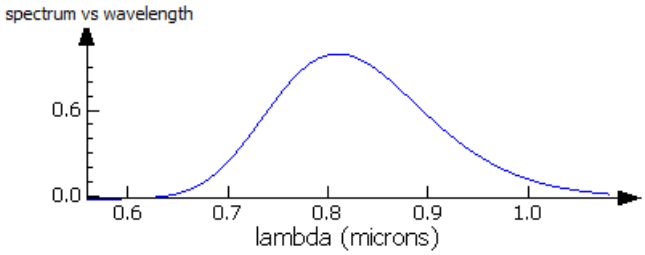

(a) The spectrum vs. wavelength graph of the simulated source in Lumerical. It is centered around 810 nm.

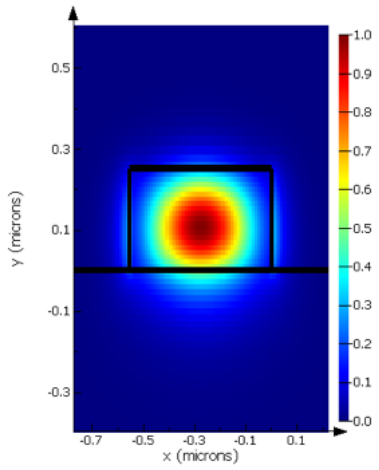

(b) A TE-mode simulation near the refractive index of SiN showing the electric field intensity inside the single waveguide.

increase of $0.05\,\mu$m and their respective refractive indices are saved. The refractive indices are then used in Eq. (3.3) to calculate the on-site energies and fit to a non-linear on-site tuning of the form

$$f(x) = A + Bx + Cx^2 + Dx^3, \tag{3.4}$$

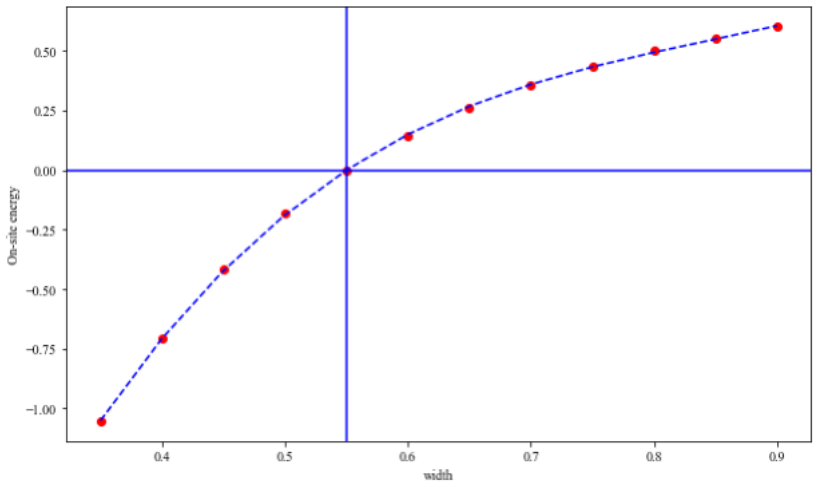

Figure 3.1.3: A fit of the on-site energy as a function of waveguide with. The zero-level is at a width of $550\,\text{nm}$.

where x is the waveguide width and $A, B, C,$ and D are parameters that are optimized (see Fig. 3.1.3). Since the design has been chosen such that the waveguides with constant width are at odd sites, and thus also on the first site, the zero-level of the fit is set to the energy of a waveguide with a width of $550\,\text{nm}$. The function with the optimized parameters are then solved for $f(x) = 0$ to get the widths x, which correspond to a linearly increasing electric field.

Next, we consider a coupled system of waveguides with different widths and calculate the propagation constants of the odd- and even modes (β^- and β^+, respectively). The difference of odd- and even-mode energies can then be calculated using

$$\Delta\beta_{coupled} = \frac{\beta^+ - \beta^-}{2}. \tag{3.5}$$

Additionally, the difference between the on-site energies of the individual waveguides are calculated using

$$\Delta\beta = \frac{\beta_1 - \beta_2}{2}, \tag{3.6}$$

where β_1 and β_2 are the on-site energies of the adjacent waveguides.

These are then used to calculate the hopping constants using

$$\mathcal{J} = \sqrt{(\Delta\beta_{coupled})^2 - (\Delta\beta)^2}. \tag{3.7}$$

Thus, using the FDFT method, two coupled waveguides are simulated, with one being that of constant width (at odd-numbered sites) and the other with varying (increasing) widths as given by the solution to Eq. (3.4). Since the coupling constant is highly dependent on the distance between the sites, a smaller gap between the waveguides will result in a larger $\mathcal{J}$, and vice versa. Thus, the waveguide gaps are iteratively adjusted to result in a constant $\mathcal{J}$ for all nearest-neighbor sites (or waveguides), which was chosen to $\mathcal{J} = 0.01 \frac{1}{\mu\text{m}}$.

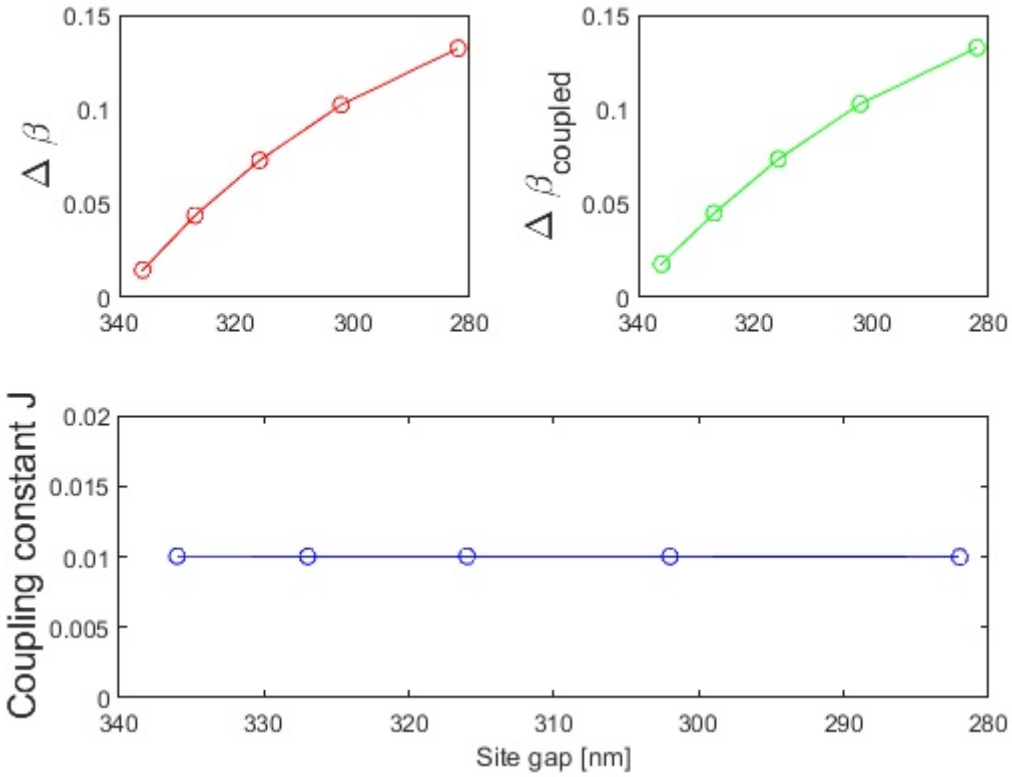

Figure 3.1.4: Plots of the resulting differences in on-site energies, propagation constants of the coupled waveguides as well as the coupling constant $\mathcal{J}$ between nearest neighbor sites as functions of the waveguide gaps.

3.2 Photonic Mosaic Lattice Fabrication

The photonic lattices used in the experiment consists of an array of eleven Si_3N_4 waveguides on top of a SiO_2 layer acting as an isolator, all on top of a silicon wafer, see Fig. A.0.1. The process includes electron beam lithography, reactive-ion etching, proximity correction, and cleaving[32, 34–37]. Further details of the fabrication process is described in Appendix A.

3.3 Experimental Procedure

The experiment was conducted using the photonic lattices of $L = 11$ coupled waveguides with single-site excitation of site numbers $3, 4$ and 6 and coupling constant of $J = 0.01 \frac{1}{\mu\text{m}}$. Two chips were used, one in the weak-force regime $F/J = 1$ (below the ME) and another in the strong-force regime (above the ME). There is a slight difference in the experimental procedure for these two cases due to their different designs, but they are mostly the same. The differences are discussed in a subsection below.

Before conducting the actual experimental procedure, we need to ensure ourselves that we excite only the fundamental TE mode of the light source. Thus, we need to eliminate the TM modes, which was done by employing a 3-paddle polarization-controller at the input light to minimize the TM mode.

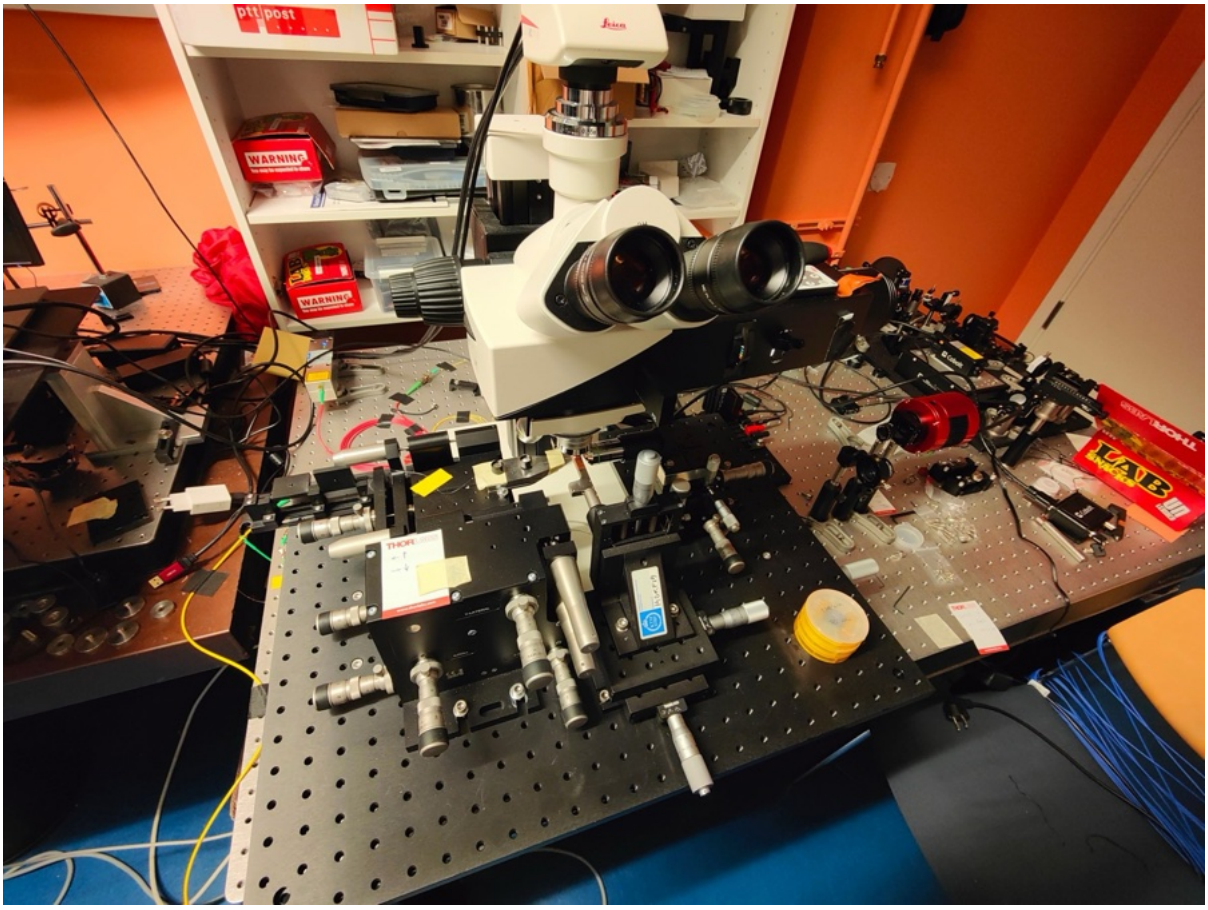

Figure 3.3.1: A photo of the experimental setup in the lab. In the photo, we can see the 6-axis nano-positioning stage in which the chip lies. Additionally, we have a 3-paddle polarization-controller at the input. To the right of the nano-positioning stage, we have a CCD camera and magnifying objective pointing toward the output light, which is also connected to a computer to observe the output light.

A schematic of the experimental procedure is illustrated in Fig. 3.3.2. A light source is

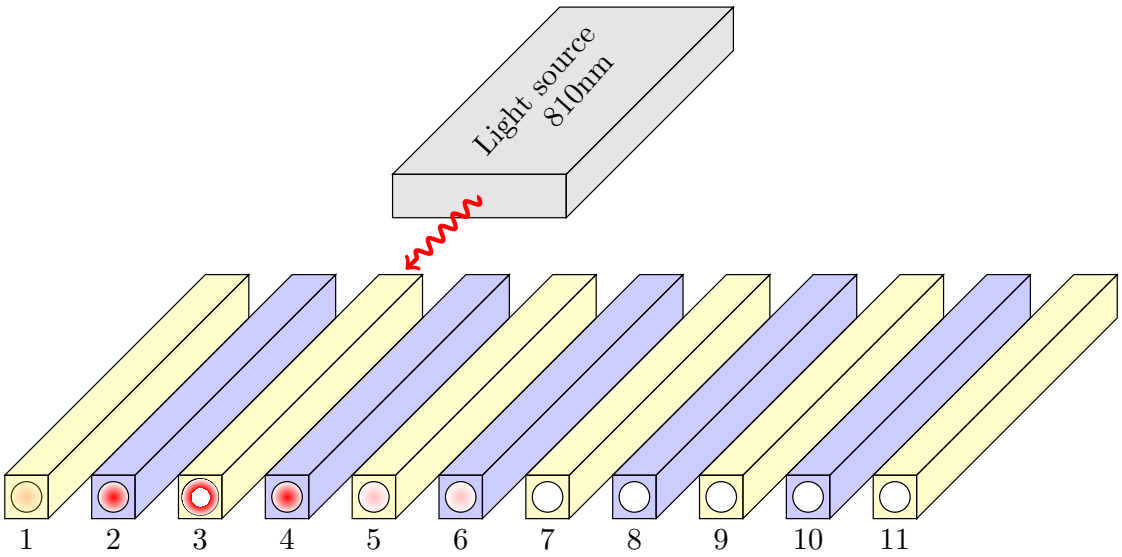

Figure 3.3.2: A simple schematic of the experimental procedure. Single-site excitation at sites 3, 4 and 6 are performed and the output light is observed using a microscope and a CCD camera. The images are saved and the light intensity profiles are analyzed.

used for single-site excitation of sites 3, 4 and 6 (only excitation of site 3 is shown in the figure). This leads to output light at the ends of the waveguides, with largest intensity at the excitation site and with a fraction of the light spreading to the neighbouring sites. To capture the light intensity profiles and analyze it, a charge-coupled device (CCD) camera with a magnifying objective is used at the output. The CCD camera saturates at a pixel value of 255, so we ensure ourselves that the highest light intensity value does not exceed 255 before saving the image.

3.4 Data Analysis Method

Once the data is collected, the next step is to analyse it to provide insight into to what degree the light intensity spreads from the excitation site to the neighbouring sites. The data is collected as images, and an example of collected images shown in Fig. 3.4.1, which corresponds to the first image in a series of images for single-site excitation of site number 3. The bright spot is the output light of site 3, and to the right of it are output of site numbers 2 and 1. Due to the large magnification, several images were collected, where the second image in the series starts from the last site of the previous image. As an example, the last site in Fig. 3.4.1 is site 4 (left of the bright spot - it is not visible in the unprocessed data image). Thus, the next image will start with

site number 4, and so on. The reason for this is that the sites farther away from the excitation site are barely visible or not visible at all, and thus we need to increase the input light intensity. In doing so, the different images are differently scaled. This is compensated by normalizing the second image in the series so that the light intensity at the starting site of the image is equal to the end-site of the previous image. In the example figure below, this corresponds to ensuring that site number 4 from the first figure (Fig. 3.4.1) is equal to the light intensity of site 4 of the next image in the series, and so on.

Next, we need a method of identifying the positions of the output light of the various sites. It is trivial to find the position of the excitation site as well as the first site in the next images (as the light intensity is increased to make it visible). However, as we can see in Fig. 3.4.1, it is not possible to identify the positions of the positions of output light of the neighbouring sites. To remedy this, we have decided to use the library called *OpenCV* which is commonly used for computer vision. The library contains functions that allow us to identify regions of light (as long as it is discernible from background noise) and providing with their coordinates. More in-depth detail of the employment of the code is described in Appendix B.

Once the positions of the output light for the different sites are found, we integrate over the light intensity of these sites on the original data image. Only one modification was done to the data image, which was to remove noise by using a threshold function similar to Eq. B.1, with the exception that values above the threshold value are kept as in the image source. Thus, values below the threshold are changed to zero, and the rest remain.

The integration area is a rectangle with user-defined dimensions - the code allows choosing width and height of the rectangle centered around the coordinates found in the previous steps, with the possibility of integrating asymmetrically by choosing width to the left and right as well as height above and below the rectangle. The sum of pixel values in the areas around the sites are saved in .txt-files for analysing. The intensities are normalized so that the total light intensity of each site is summed to 1.

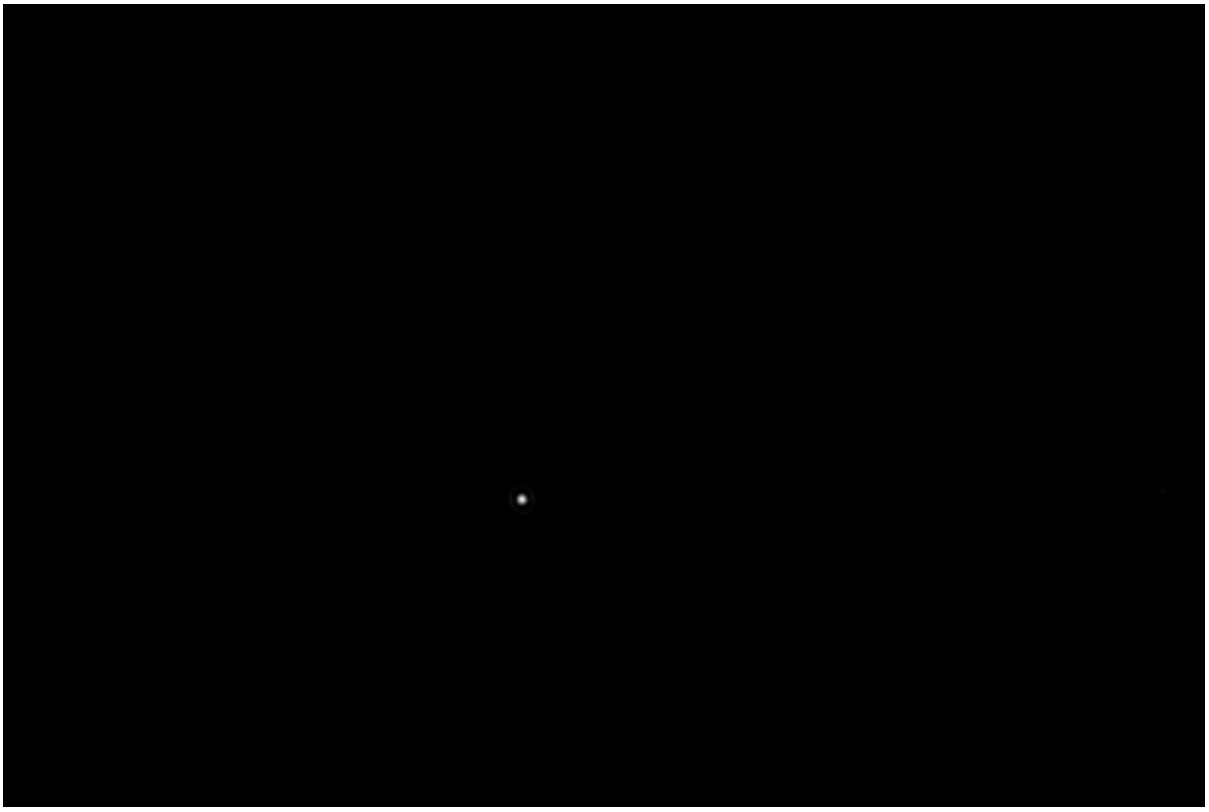

Figure 3.4.1: An example of the collected data images. This image is the light intensity output for single-site excitation of site number 3, where the bright spot corresponds to site 3.

3.5 Differences in device structures

There are slight differences in the devices used for the weak-force and strong-force regimes. These differences are summarized in Table 3.5.1. Due to the lower magnification used in the weak-force regime, all the sites were captured in one image from the CCD camera. This made the image processing much simpler, as it eliminated the need for scaling several images of various sites from the same single-site excitation.

	Weak-force regime	Strong-force regime
Input light wavelength	786 nm	810 nm
Position of CCD camera	Top-down	Facet-side
Magnification Objective	40X	100X

Table 3.5.1: Summary of the differences between the devices for the weak-force regime and strong-force regime.

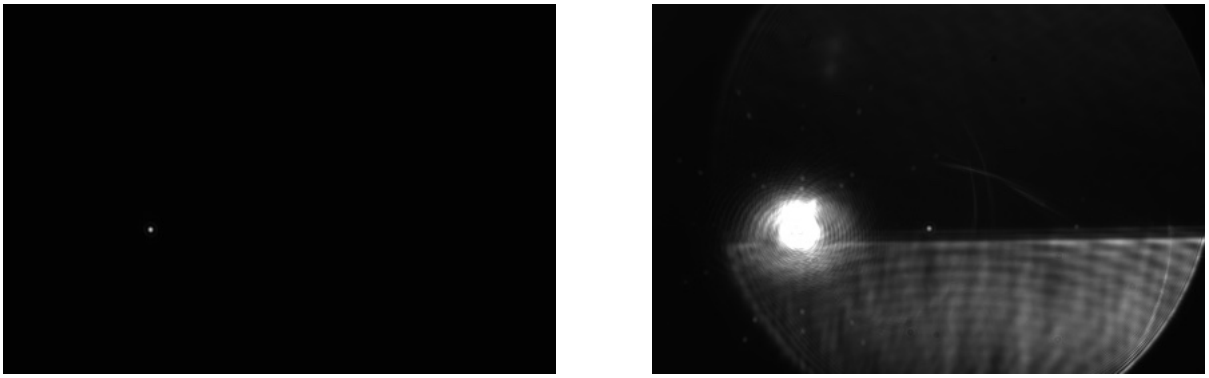

(a) Data image used in the analysis (b) Reference image

Figure 3.4.2: Illustration of the output data images for excitation of site number 6. The data image is in (a), and a reference image is shown in (b), which was used to identify the neighbouring sites.

Chapter 4

Result

The data images that are collected, as described in sec. 3.4, are processed and the light intensity profiles are analysed for the weak-force regime ($F/J = 1$) and strong-force regime ($F/J = 4$). The following sections present the results following the data analysis in both of these regimes.

4.1 Theoretical solutions

The model Hamiltonian as described in Eq. (2.12) was solved with the parameters used in the experiment, i.e. $\kappa = 2$ and $L = 11$ sites. This is illustrated in Fig. 4.1.1, with the pseudo ME in finite size lattice and the weak-force and strong-force regimes highlighted. To the sides, we have the theoretical intensity profiles of the weak-force regime (left) and strong-force regime (right). The calculations were done numerically in Python utilizing the QuTiP (Quantum Toolbox in Python) library, which allows creating Hamiltonians, state vectors, eigenenergy solutions, and more.

4.2 Light Intensity Profile

The image data processing as explained in 3.4 and Appendix B results in light intensity profiles for both the strong- and weak-force regimes for various excitation sites. Here, we present the results for both these regimes. For plots in both these regimes, we use logarithmic scale in the y-axis and with the same ticks to elucidate their differences and expedite comparisons between the two. It is also crucial to compare them with the theoretical solutions as shown in Fig. 4.1.1.

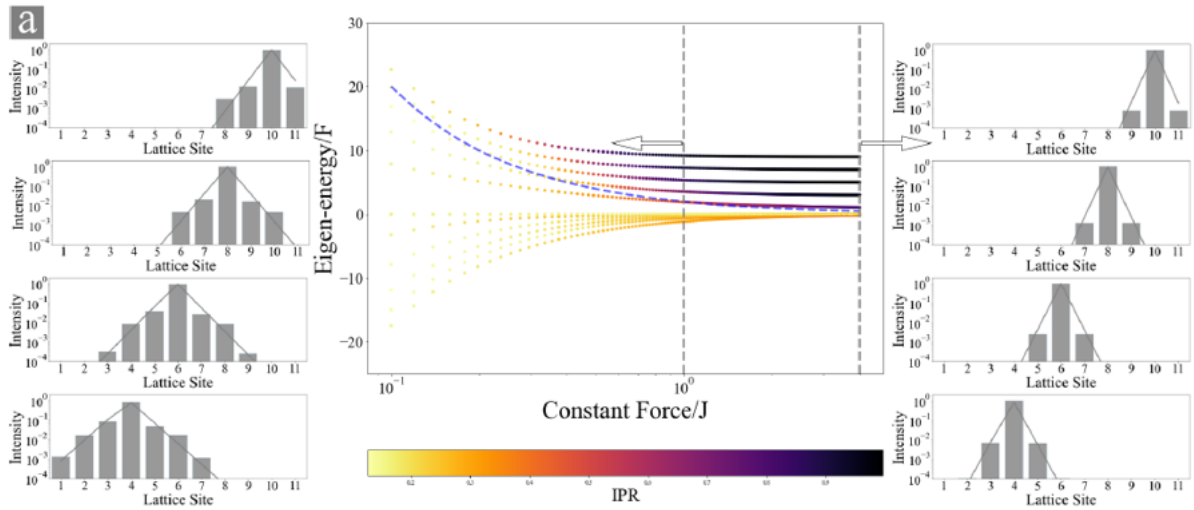

Figure 4.1.1: The theoretical eigenenergy values for $\kappa = 2$ with $L = 11$ and with the strong-force regime ($F/J = 4$) and weak-force regime ($F/J = 1$) highlighted. Additionally, the theoretically expected intensity profiles are to the left (weak-force regime) and right (strong-force regime) for comparison with the experimental intensity profiles.

4.2.1 Weak-force Regime

The intensity distributions for the weak-force regime at excitation sites 4 and 6 are summarized in Fig. 4.2.1. In both the cases, spreading of light is observed, with around $5 \cdot 10^{-2}$ of the intensity at each site. Total integration area is 3500 around each site.

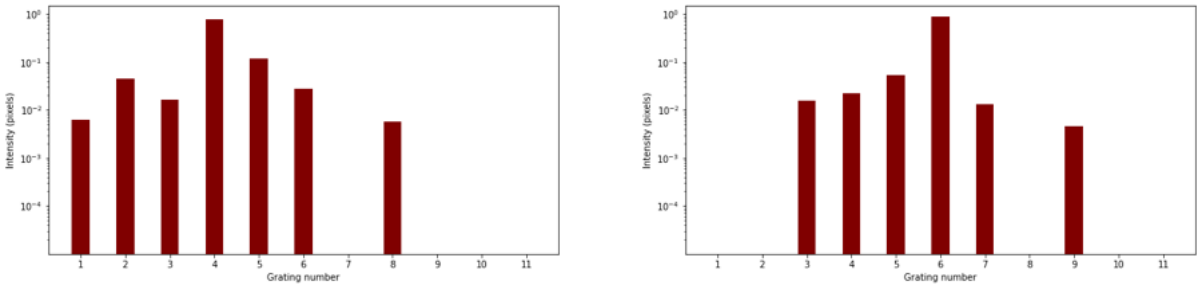

(a) (b)

Figure 4.2.1: Normalized light intensities in logarithmic scale for light excitation of site number (a) 4 and (b) 6 in the weak-force regime.

4.2.2 Strong-force regime

The analysed data of the strong-force regime were analysed and the light intensity distribution is summarized in Fig. 4.2.2. The total integration area was the same

	Intensity	
Site \ Excitation Site	4	6
1	0.00625197	0
2	0.044692	0
3	0.0163392	0.0159474
4	0.781776	0.022356
5	0.117579	0.0529913
6	0.0277398	0.891035
7	0	0.013058
8	0.00562152	0
9	0	0.00461197
10	0.040999	0
11	0.040999	0

Table 4.2.1: The resulting intensities at each site for various excitation sites in the strong-force regime. The intensities are normalized so that the total intensity is 1. Excitation-site intensities are highlighted in blue for clarity.

(81000 pixels) for all the cases. We notice that the light intensity is much less localized at the excitation site 3 in (a) than excitation sites 4 and 6 in (b) and (c), respectively. Light intensity at site 2 in (a), the nearest-neighbor site, is approximately $2 \cdot 10^{-2}$, while in (b) light intensity of site 3 (nearest neighbor to excitation site 4) is roughly $2 \cdot 10^{-3}$, or about a tenth of the intensity of the relative intensity of site 2 in (a). Moreover, no light intensity was observed at neighbouring sites for excitation of site 6 as shown in Fig. 4.2.2c.

	Intensity		
Site \ Excitation Site	3	4	6
1	0.00373	0	0
2	0.0235	0	0
3	0.949	0.00242	0
4	0.000622	0.998	0
5	0.0111	0.0000293	0
6	0.00376	0	1
7	0.00497	0	0
8	0.00354	0	0
9	0	0	0
10	0	0	0
11	0	0	0

Table 4.2.2: The resulting intensities at each site for various excitation sites in the strong-force regime. The intensities are normalized so that the total intensity is 1. Excitation-site intensities are highlighted in blue for clarity.

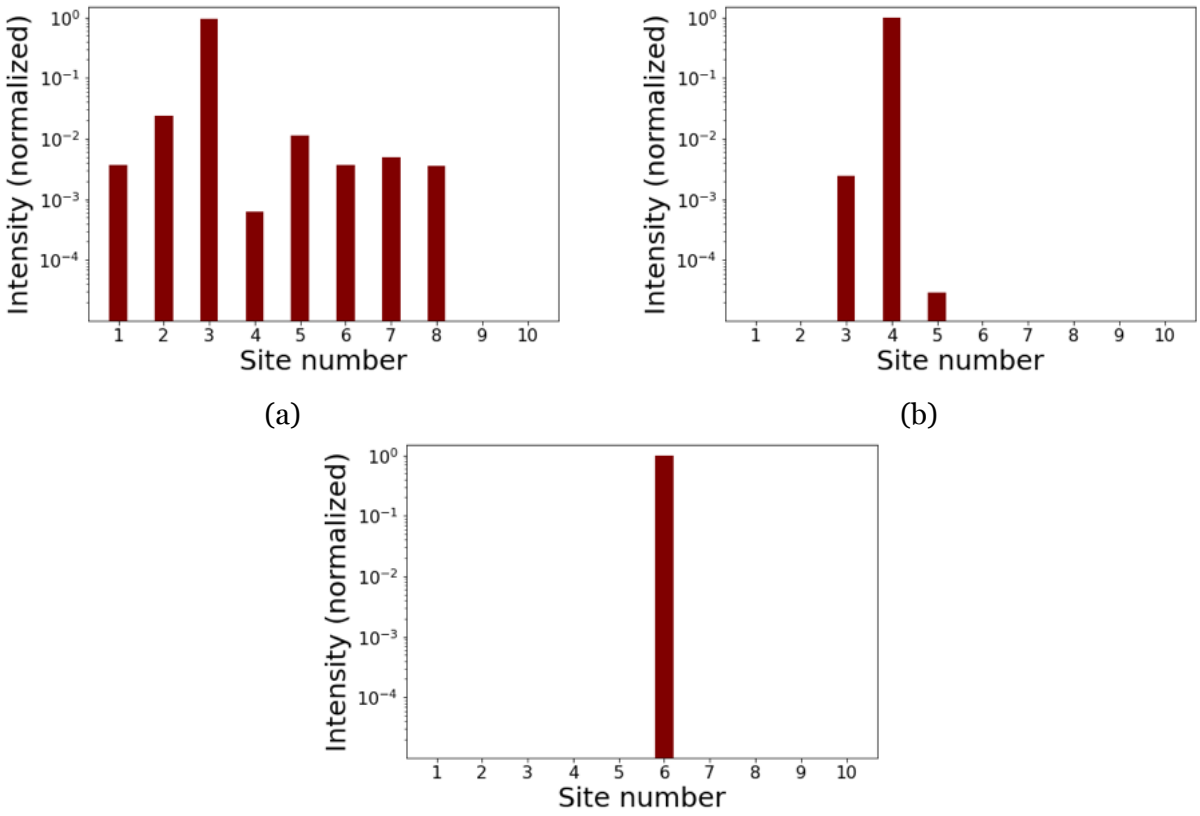

Figure 4.2.2: Normalized light intensities in logarithmic scale for inputs (a) 3 (b) 4 and (c) 6. No light intensity could be distinguished from the scattered noise in input 6. Notice that site 5 in (a) has a higher intensity (despite being next-to-nearest-neighbor site) than input 3 in (b), the nearest-neighbor site.

Chapter 5

Discussions & Conclusions

This chapter of the thesis work focuses on discussions and conclusions based on the results and methodology, and potential future work/experiments related to the thesis are discussed.

5.1 Discussion

The results of the light intensity profile as presented in 4.2 strongly indicate a phase transition from extended to localized states of the even-numbered sites 4 and 6 from the weak-force regime to the strong-force regime, and thereby indicating the existence of an ME in the disorder-free photonic lattice.

Clearly, there are some limitations to the experiment, specifically in the device used for the strong-force regime, as it was not possible to integrate over all the sites due to limitations of the CCD camera, which saturates at light intensity corresponding to pixel values of 255, combined with the use of a 100X magnifying objective preventing us from observing all the sites in one image. Additionally, the noise due to light scattering significantly increased on the bottom part of the image when the light intensity was increased to make the sites far from the excitation site visible. However, these limitations mainly affect exact light intensity profiles. Since we are mainly interested in the degree at which the light spreads from the excitation site to the neighbouring sites, and since there is a significant difference in the spreading compared to the weak-force regime (about $\frac{1}{10}$ of the intensity at site 3 for excitation of site 4 between the strong-field regime and weak-field regime, see Figs. 4.2.1 and 4.2.2), the effects of these

limitations are not significant enough. The issue of the noise from scattering of light should affect all sites on average equally, and so will not be relevant when normalized. Moreover, a significant increase in input light intensity was necessary to observe light on neighbouring sites for the even-numbered excitation sites (4 and 6), and quickly became so large that it was overshadowed by the scattering noise. This is clear in Fig. 3.4.2b, which was used as a reference to identify neighbouring sites. This was necessary because the light intensity in the neighbouring sites were significantly weaker such that they were not identifiable with the data analysis method described in Appendix B. In the figure, we see the significant scattering of light on the bottom part and a weak spot of light at site number 5. Note that the light intensity was increased significantly, and yet only the nearest neighbouring site was visible. For the original image used for the data analysis (Fig. 3.4.2a), this yielded zero intensity even at site number 5. Because of saturation of the CCD camera, this means that the intensity at site 5 (and also 4) for excitation of site 6 should have an intensity less than $1/255 \approx 4 \cdot 10^{-3}$ (since maximum pixel value is 255). This is also consistent with the theoretical expectation as illustrated to the right side of Fig. 4.1.1.

Moreover, for the light intensity of sites $9-10$ for excitation of site 3 (Fig. 4.2.2a), there was light scattering on and around these sites. Since it was not possible to remove the scattered light without affecting the output light of the sites, they were instead omitted and is the reason why the results show zero intensity.

Lastly, for the strong-force regime, a fabrication error resulted in site number 11 not being included in the chip, as can be seen in Fig. 5.1.1. However, this would not have affected the results in any way, since no light was observed for sites beyond nearest-neighbour sites for excitation of sites 4 and 6, and sites 9 and above for excitation of site 3 were indistinguishable from scattered light. Additionally, the intensity at site 11 for excitation of site number 3 is expected to be extremely small, which can be seen in the weak-force regime (left) of Fig. 4.1.1. While excitation site number 3 is not included there, it suffices to observe that for excitation of site number 4, the intensity at site 11 is very small.

It is also noteworthy that when comparing Fig. 4.2.2b with Fig. 4.2.2c, it appears as if site 4 is less localized than site 6. This is actually expected from the theoretical calculations, since the eigenenergy of site 6 is larger than the eigenenergy of site 4, and thus being ”farther” away from the ME in energy. In Fig. 4.1.1, this corresponds to site

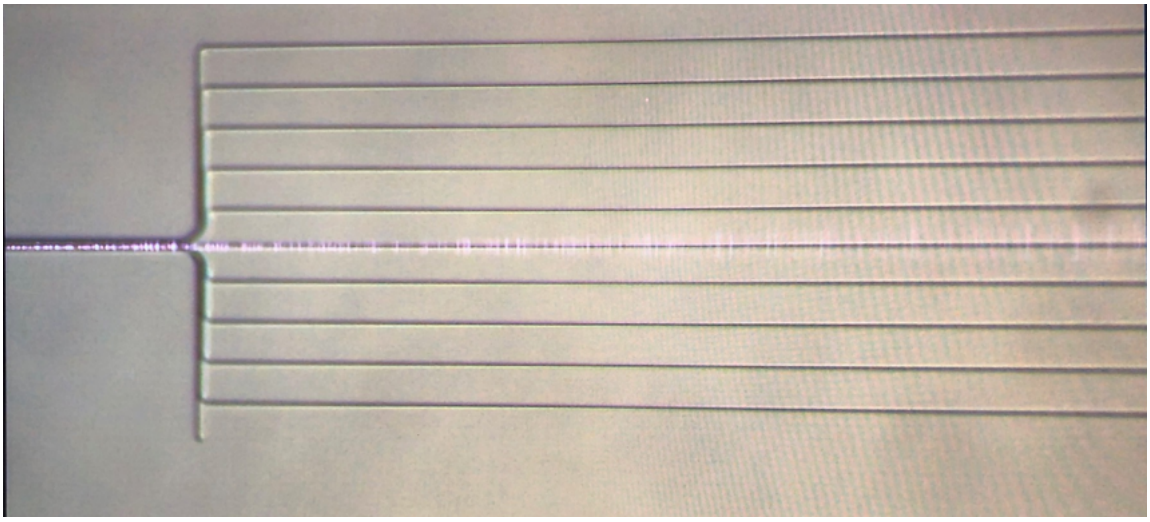

Figure 5.1.1: Image of the device used for the strong-force regime highlighting the missing 11^{th} waveguide and light propagation through site 6.

4 having a lower value of IPR than site 6, making it less localized.

5.2 Conclusion

By fabricating two devices, one for the weak-force regime and one for the strong-force regime, we have observed the intensity profiles of the output light in the disorder-free photonic lattices, with a strong indication of the existence of a phase transition and hence a ME. The weak-force regime exhibits extended states for excitation of sites 4 and 6, while the strong-force regime show significantly decreased spreading of light (localized states) for excitation of the same sites.

Moreover, it can also be concluded that top-down camera is generally better to avoid scattering of light, which only occurred on the bottom part for the facet-side observation (as used in the device for the strong-field regime). It is especially beneficial to use a magnification objective that allows observation of all the sites in one image, as this simplifies the data and image processing.

5.2.1 Future Work

The experimental method used to observe ME in the disorder-free lattices was with classical light in photonic lattices to simulate the 1D quantum transport of electrons. Future work could build on the work in this thesis in various ways. For example, it is interesting to investigate whether the experiment can be generalized to a 2-

dimensional lattice. In a paper by Yuchen Wang, et al. [38], the ME in a 2D vertex-decorated Lieb lattice with quasi-periodic potential was calculated. While this is not a disorder-free lattice, a similar procedure could be used to simulate a quasi-periodic potential. Engineering such a device might not be trivial, though.

Additionally, the quantum properties of light in the devices used in this thesis work may be especially interesting to investigate. Such an experiment may be realized for example using single-photon sources and superconducting nanowire single-photon detector (SNSPD) to investigate various quantum properties, such as entanglement or the Hong-Ou-Mandel effect.

Bibliography

[1] Wikipedia contributors. *Quantum technology — Wikipedia, The Free Encyclopedia*. [Online; accessed 8-May-2023]. 2023. URL: https://en.wikipedia.org/w/index.php?title=Quantum_technology&oldid=1152630985.

[2] "Pioneering quantum information science". In: *Nature Computational Science* 2.11 (Nov. 2022), pp. 687–688. ISSN: 2662-8457. DOI: 10.1038/s43588-022-00368-0. URL: https://doi.org/10.1038/s43588-022-00368-0.

[3] Moody, Galan, Sorger, Volker J, Blumenthal, Daniel J, Juodawlkis, Paul W, Loh, William, Sorace-Agaskar, Cheryl, Jones, Alex E, Balram, Krishna C, Matthews, Jonathan CF, Laing, Anthony, et al. "2022 roadmap on integrated quantum photonics". In: *Journal of Physics: Photonics* 4.1 (2022), p. 012501.

[4] Gao, Jun, Santos, Leonardo, Krishna, Govind, Xu, Ze-Sheng, Iovan, Adrian, Steinhauer, Stephan, Gühne, Otfried, Poole, Philip J, Dalacu, Dan, Zwiller, Val, et al. "Scalable generation and detection of on-demand W states in nanophotonic circuits". In: *Nano Letters* (2023).

[5] Elshaari, Ali W, Pernice, Wolfram, Srinivasan, Kartik, Benson, Oliver, and Zwiller, Val. "Hybrid integrated quantum photonic circuits". In: *Nature Photonics* (2020), pp. 1–14.

[6] Clarke, James S. *An Optimist's View of the 4 Challenges to Quantum Computing*. https://spectrum.ieee.org/an-optimists-view-of-the-4-challenges-to-quantum-computing. Accessed: 2023-05-08.

[7] Zadeh, Iman Esmaeil, Elshaari, Ali W, Jöns, Klaus D, Fognini, Andreas, Dalacu, Dan, Poole, Philip J, Reimer, Michael E, and Zwiller, Val. "Deterministic integration of single photon sources in silicon based photonic circuits". In: *Nano letters* 16.4 (2016), pp. 2289–2294.

[8] Elshaari, Ali W, Büyüközer, Efe, Zadeh, Iman Esmaeil, Lettner, Thomas, Zhao, Peng, Schöll, Eva, Gyger, Samuel, Reimer, Michael E, Dalacu, Dan, Poole, Philip J, et al. "Strain-tunable quantum integrated photonics". In: *Nano letters* 18.12 (2018), pp. 7969–7976.

[9] Elshaari, Ali W, Zadeh, Iman Esmaeil, Fognini, Andreas, Reimer, Michael E, Dalacu, Dan, Poole, Philip J, Zwiller, Val, and Jöns, Klaus D. "On-chip single photon filtering and multiplexing in hybrid quantum photonic circuits". In: *Nature communications* 8.1 (2017), p. 379.

[10] Steinhauer, Stephan, Versteegh, Marijn AM, Gyger, Samuel, Elshaari, Ali W, Kunert, Birgit, Mysyrowicz, André, and Zwiller, Val. "Rydberg excitons in Cu2O microcrystals grown on a silicon platform". In: *Communications Materials* 1.1 (2020), p. 11.

[11] Gyger, Samuel, Zichi, Julien, Schweickert, Lucas, Elshaari, Ali W, Steinhauer, Stephan, Covre da Silva, Saimon F, Rastelli, Armando, Zwiller, Val, Jöns, Klaus D, and Errando-Herranz, Carlos. "Reconfigurable photonics with on-chip single-photon detectors". In: *Nature communications* 12.1 (2021), p. 1408.

[12] Errando-Herranz, Carlos, Schöll, Eva, Picard, Raphaël, Laini, Micaela, Gyger, Samuel, Elshaari, Ali W, Branny, Art, Wennberg, Ulrika, Barbat, Sebastien, Renaud, Thibaut, et al. "Resonance Fluorescence from Waveguide-Coupled, Strain-Localized, Two-Dimensional Quantum Emitters". In: *ACS Photonics* (2021).

[13] Chang, Jin, Gao, Jun, Esmaeil Zadeh, Iman, Elshaari, Ali W, and Zwiller, Val. "Nanowire-based integrated photonics for quantum information and quantum sensing". In: *Nanophotonics* 12.3 (2023), pp. 339–358.

[14] Gladchenko, Sergey, Olaya, David, Dupont-Ferrier, Eva, Douçot, Benoit, Ioffe, Lev B., and Gershenson, Michael E. "Superconducting nanocircuits for topologically protected qubits". In: *Nature Physics* 5.1 (Jan. 2009), pp. 48–53. ISSN: 1745-2481. DOI: 10.1038/nphys1151. URL: https://doi.org/10.1038/nphys1151.

[15] Anderson, P. W. "Absence of Diffusion in Certain Random Lattices". In: *Phys. Rev.* 109 (5 Mar. 1958), pp. 1492–1505. DOI: 10.1103/PhysRev.109.1492. URL: https://link.aps.org/doi/10.1103/PhysRev.109.1492.

[16] Girvin, Steven M. and Yang, Kun. *Modern Condensed Matter Physics*. Cambridge University Press, 2019. DOI: 10.1017/9781316480649.

[17] Dwiputra, Donny and Zen, Freddy P. "Single-particle mobility edge without disorder". In: *Phys. Rev. B* 105 (8 Feb. 2022), p. L081110. DOI: 10.1103/PhysRevB.105.L081110. URL: https://link.aps.org/doi/10.1103/PhysRevB.105.L081110.

[18] Longhi, Stefano. "Absence of mobility edges in mosaic Wannier-Stark lattices". In: *Phys. Rev. B* 108 (6 Aug. 2023), p. 064206. DOI: 10.1103/PhysRevB.108.064206. URL: https://link.aps.org/doi/10.1103/PhysRevB.108.064206.

[19] Longhi, S. "Quantum-optical analogies using photonic structures". eng. In: *Laser & photonics reviews* 3.3 (2009), pp. 243–261. ISSN: 1863-8880.

[20] Lahini, Yoav, Avidan, Assaf, Pozzi, Francesca, Sorel, Marc, Morandotti, Roberto, Christodoulides, Demetrios N., and Silberberg, Yaron. "Anderson Localization and Nonlinearity in One-Dimensional Disordered Photonic Lattices". In: *Phys. Rev. Lett.* 100 (1 Jan. 2008), p. 013906. DOI: 10.1103/PhysRevLett.100.013906. URL: https://link.aps.org/doi/10.1103/PhysRevLett.100.013906.

[21] Marzari, Nicola and Vanderbilt, David. "Maximally localized generalized Wannier functions for composite energy bands". In: *Phys. Rev. B* 56 (20 Nov. 1997), pp. 12847–12865. DOI: 10.1103/PhysRevB.56.12847. URL: https://link.aps.org/doi/10.1103/PhysRevB.56.12847.

[22] Wannier, Gregory H. "Dynamics of band electrons in electric and magnetic fields". eng. In: *Reviews of modern physics* 34.4 (1962), pp. 645–655. ISSN: 0034-6861.

[23] Fukuyama, Hidetoshi, Bari, Robert A., and Fogedby, Hans C. "Tightly Bound Electrons in a Uniform Electric Field". eng. In: *Physical review. B, Solid state* 8.12 (1973), pp. 5579–5586. ISSN: 0556-2805.

[24] Mendez, E.E., Agullã-Rueda, F., and Hong, J.M. "Stark localization in GaAs-GaAlAs superlattices under an electric field". eng. In: *Physical review letters* 60.23 (1988), pp. 2426–2429. ISSN: 0031-9007.

[25] Voisin, P., Bleuse, J., Bouche, C., Gaillard, S., Alibert, C., and Regreny, A. "Observation of the Wannier-Stark quantization in a semiconductor superlattice". eng. In: *Physical review letters* 61.14 (1988), pp. 1639–1642. ISSN: 0031-9007.

[26] Abrahams, E., Anderson, P.W., Licciardello, D.C., and Ramakrishnan, T.V. “Scaling theory of localization: Absence of quantum diffusion in two dimensions”. eng. In: *Physical review letters* 42.10 (1979), pp. 673–676. ISSN: 0031-9007.

[27] Das Sarma, S., He, Song, and Xie, X.C. “Mobility edge in a model one-dimensional potential”. eng. In: *Physical review letters* 61.18 (1988), pp. 2144–2147. ISSN: 0031-9007.

[28] Liu, Tong, Yan, Hai-Yang, and Guo, Hao. “Fate of topological states and mobility edges in one-dimensional slowly varying incommensurate potentials”. eng. In: *Physical review. B* 96.17 (2017). ISSN: 2469-9950.

[29] Biddle, J., Wang, B., Priour, D.J., and Das Sarma, S. “Localization in one-dimensional incommensurate lattices beyond the Aubry-André model”. eng. In: *Physical review. A, Atomic, molecular, and optical physics* 80.2 (2009). ISSN: 1050-2947.

[30] Wang, Yucheng, Xia, Xu, Zhang, Long, Yao, Hepeng, Chen, Shu, You, Jiangong, Zhou, Qi, and Liu, Xiong-Jun. “One-Dimensional Quasiperiodic Mosaic Lattice with Exact Mobility Edges”. eng. In: *Physical review letters* 125.19 (2020), pp. 1–196604. ISSN: 0031-9007.

[31] Wei, Xingbo, Wu, Liangqing, Feng, Kewei, Liu, Tong, and Zhang, Yunbo. “Exact mobility edges in finite-height Wannier-Stark ladders”. In: *arXiv preprint arXiv:2308.15516* (2023).

[32] Gao, Jun, Khaymovich, Ivan M, Iovan, Adrian, Wang, Xiao-Wei, Krishna, Govind, Xu, Ze-Sheng, Tortumlu, Emrah, Balatsky, Alexander V, Zwiller, Val, and Elshaari, Ali W. “Coexistence of extended and localized states in finite-sized mosaic Wannier-Stark lattices”. In: *Physical Review B* 108.14 (2023), p. L140202.

[33] Nevlacsil, Stefan, Eggeling, Moritz, Muellner, Paul, Koppitsch, Guenther, Sagmeister, Martin, Kraft, Jochen, and Hainberger, Rainer. “Broadband SiN asymmetric directional coupler for 840 nm operation”. In: *OSA Continuum* 1.4 (Dec. 2018), pp. 1324–1331. DOI: 10.1364/OSAC.1.001324. URL: https://opg.optica.org/osac/abstract.cfm?URI=osac-1-4-1324.

[34] Gao, Jun, Xu, Ze-Sheng, Smirnova, Daria A, Leykam, Daniel, Gyger, Samuel, Zhou, Wen-Hao, Steinhauer, Stephan, Zwiller, Val, and Elshaari, Ali W. “Observation of Anderson phase in a topological photonic circuit”. In: *Physical Review Research* 4.3 (2022), p. 033222.

[35] Xu, Ze-Sheng, Gao, Jun, Krishna, Govind, Steinhauer, Stephan, Zwiller, Val, and Elshaari, Ali W. “Direct measurement of topological invariants in photonic superlattices”. In: *Photonics Research* 10.12 (2022), pp. 2901–2907.

[36] Gao, Jun, Khaymovich, Ivan M, Wang, Xiao-Wei, Xu, Ze-Sheng, Iovan, Adrian, Krishna, Govind, Balatsky, Alexander V, Zwiller, Val, and Elshaari, Ali W. “Experimental probe of multi-mobility edges in quasiperiodic mosaic lattices”. In: *arXiv preprint arXiv:2306.10829* (2023).

[37] Xu, Ze-Sheng, Gao, Jun, Iovan, Adrian, Khaymovich, Ivan M, Zwiller, Val, and Elshaari, Ali W. “Observation of reentrant metal-insulator transition in a random-dimer disordered SSH lattice”. In: *arXiv preprint arXiv:2307.05207* (2023).

[38] Wang, Yucheng, Zhang, Long, Wan, Yuhao, He, Yu, and Wang, Yongjian. “Two-dimensional vertex-decorated Lieb lattice with exact mobility edges and robust flat bands”. In: *Phys. Rev. B* 107 (14 Apr. 2023), p. L140201. DOI: 10.1103/PhysRevB.107.L140201. URL: https://link.aps.org/doi/10.1103/PhysRevB.107.L140201.

Appendix - Contents

A Photonic Mosaic Lattice Fabrication **36**

B Image processing **38**

B.1 Identification of bright spots 38

B.2 Light intensity integration 39

Appendix A

Photonic Mosaic Lattice Fabrication

The photonic lattice fabrication is initiated by covering Si wafers with a $3.3\,\mu$m insulating layer of SiO_2 and a 250 nm layer of Si_3N_4 acting as the waveguides. The next step involves patterning the waveguides to the desired shapes. This was done using electron beam lithography, where a negative-tone resist is laid on top of the Si_3N_4 layer followed by directing an electron beam onto the resist and thereby hardening these regions. The unexposed regions are then removed using a developer solution, which result in a patterned layer of resist. The resist layer is then used as a mask for dry etching of the Si_3N_4, which was done using a CF_4-based reactive ion etching technique. This allows us to remove Si_3N_4 layer that are exposed (not covered by the resist), forming waveguides with the desired dimensions and shapes.

Lastly, we make sure to remove the remaining electron-beam resist is removed by using a resist remover solution, clean and dry the samples. An illustration of the fabrication steps are shown in Fig. A.0.1, as well as microscope images of the fabricated structures in Fig. A.0.2.

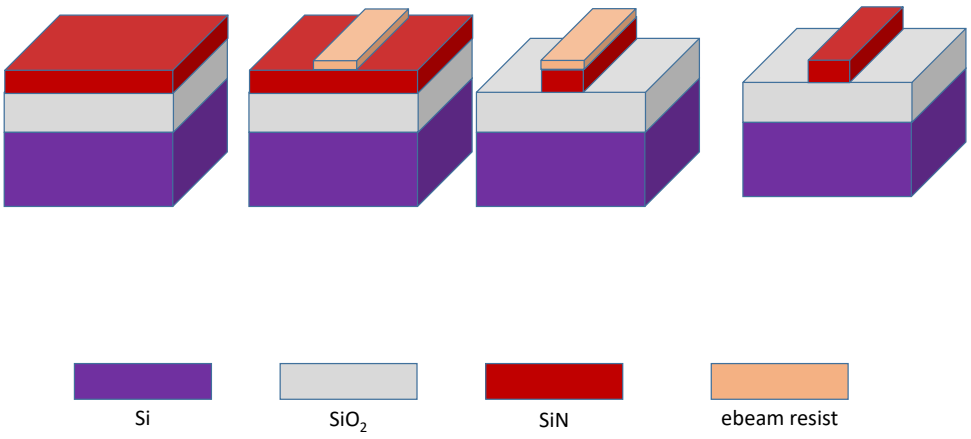

Figure A.0.1: Illustration of the fabrication process of the coupled Si_3N_4 photonic lattices.

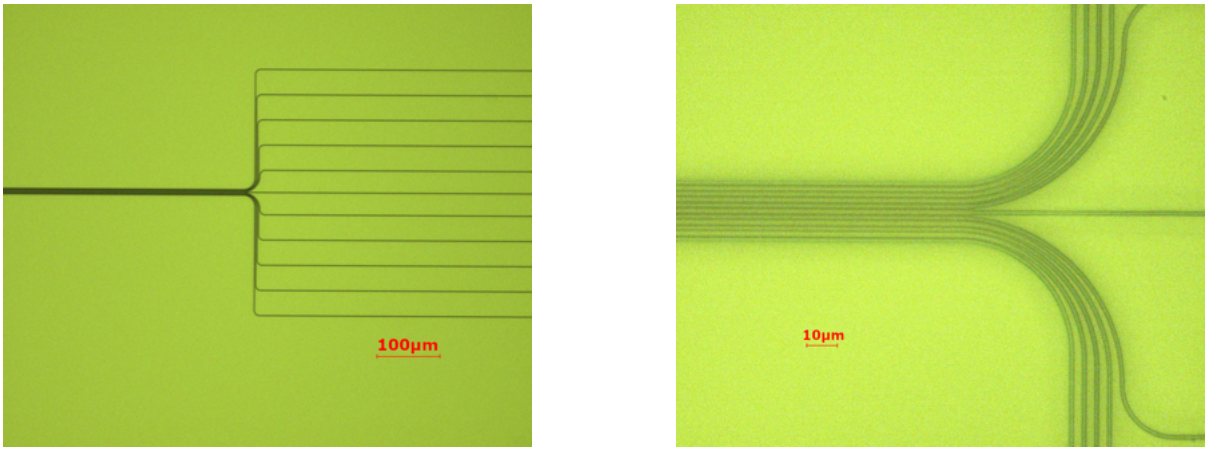

(a) (b)

Figure A.0.2

Appendix B

Image processing

In sec. 3.4 the data analysis method was explained and an example of a data image was shown in Fig. 3.4.1. Because of the difficulty of finding the bright areas from the output light of the neighbouring sites, we need to use other methods than the naked eye. Thus, we have to process the images.

The image processing consists of 2 central steps, namely 1. identification of bright spots that result from the output of the waveguides and 2. integration (summation) of pixel values around these sites. The first step is performed using the library OpenCV.

B.1 Identification of bright spots

Identifying the bright spots require several steps of manipulation of the image. The images in Fig. B.1.1 illustrate the steps explained below, and are performed on single-site excitation of site number 3, as in Fig. 3.4.1.

1. *Blurring* of the image to reduce high frequency noise with gaussian blur.
2. *Thresholding* to create a large contrast between noise and the bright spots. Mathematically, the threshold function works as follows:

$$f(x,y) = \begin{cases} maxval, & \text{if } src(x,y) > threshold, \\ 0, & \text{otherwise}, \end{cases} \tag{B.1}$$

   where $src(x,y)$ is the source image and $threshold$ is a chosen threshold value.

Thus, if the pixel value is above the threshold value, it will be changed to the maximum value, which was chosen to 255. Otherwise, it will be converted to 0, and hence removing noise. For most of the images, the threshold value was chosen to be 2. For images with large degree of noise or light scattering, a higher threshold value was chosen, but the drawback was that weak light from the sites would then disappear together with the noise.

3. *Erosion and dilation* - two functions in the OpenCV library that removes noise that arise from the thresholding, mainly around the site areas. By ”eroding” light around the sites, we remove small blobs of light. Dilation, then, increases the radius of the bright spot so that any remaining noise becomes part of the full component of the light from the site.

4. *Connected-component analysis* is a follow-up from the previous function, which removes spots of light that are smaller than a user-defined value of pixels inside an area around the bright spots. Thus, only large enough ”spots” are kept, and their coordinates, as well as the minimum radius that encircles the bright spot.

5. *Labeling* is the last step of the identification. The saved coordinates and radii are used to create circles in the image around the bright spots. Additionally, a function from the package *imutils*, namely *imutils.contours.sortcontours()* is used to sort the blobs from right-to-left, which allows us to label them according to their site numbers (increasing site number from right-to-left).

B.2 Light intensity integration

Once the bright blobs/spots have been identified, we use the coordinates to integrate in a rectangle around the sites. The rectangular area’s dimension can be chosen; both the width to the left and right as well as the height on the top and bottom relative to the center coordinates. It is important to note that the area is constant for all the images in the weak-force and strong-force cases. Upon trial-and-error process, the dimensions were chosen as shown in table B.2.1. Here, the values indicate pixels relative to the center coordinates. For example, in the weak-force regime, we have width (left) as 100, meaning that the left side of the rectangle is 100 pixels to the left of the center. Due to the large amount of scattering of light below the sites, we have chosen an asymmetric height, where the bottom part of the integration area is closer to the center (120 pixels

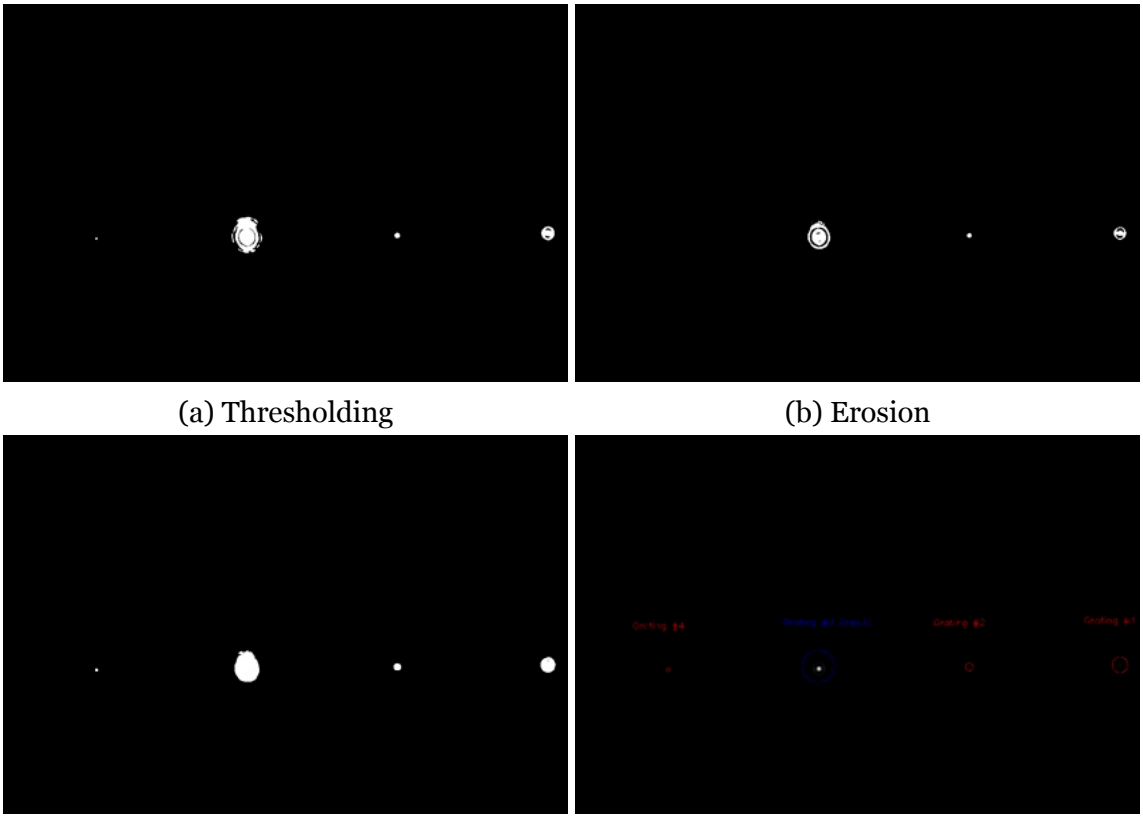

(a) Thresholding (b) Erosion

(c) Dilation (d) Labeling

Figure B.1.1: Images illustrating the steps of identifying the bright spots that arise from the output light of the various sites. The processed images are all the first image in the series of single-site excitation of site number 3.

below the center) as opposed to the top part, which (150 pixels above the center), see Fig. B.2.1.

	Strong-force	Weak-force
width (left)	150	100
width (right)	150	100
height (top)	150	35
height (bottom)	120	35
Area	81000	3500

Table B.2.1: The chosen dimensions of the integration area as well as the total area for both the weak-force and the strong-force regimes.

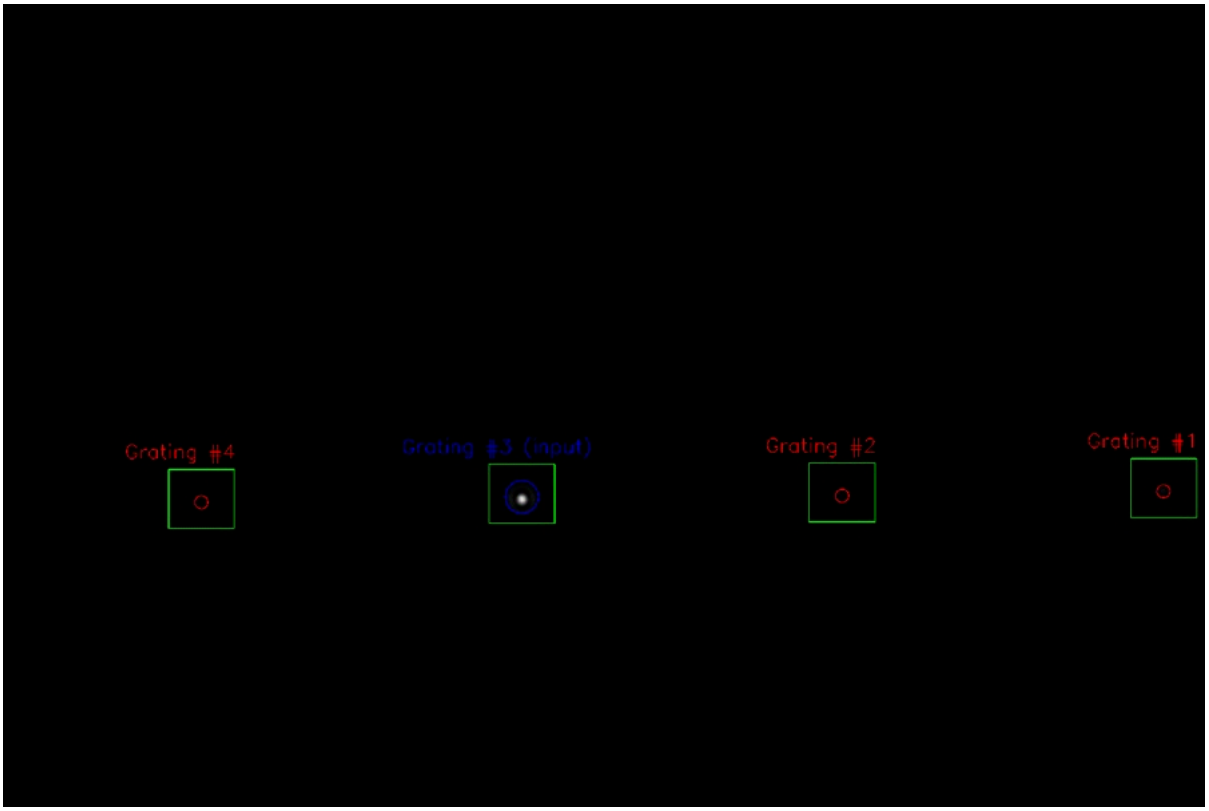

Figure B.2.1: Illustration of the integration area around the identified bright spots.